New Insights into Coupled Frequency Dynamics of AC Grids in Rectifier and Inverter Side of LCC-HVDC Interfacing DFIG-based Wind Farms

Sai Gopal Vennelaganti, *Student Member, IEEE*, and Nilanjan Ray Chaudhuri, *Senior Member, IEEE*

***Abstract*—Coupling between frequency dynamics of the AC systems on both inverter and rectifier side of LCC-HVDC with the rectifier station operating in frequency control is studied, along with the presence of large DFIG-based wind farms on the weak rectifier-side grid. An averaged model with seventy nine states, which includes dynamic models of grids on rectifier and inverter sides, phase-lock-loop, and the wind farm is derived. To develop a deeper understanding of the frequency dynamics, a simplified four-state nonlinear model is proposed, which in turn reveals a strong coupling between frequency and AC voltage at the HVDC rectifier terminal. A firing angle correction strategy is proposed to decouple frequency-voltage interactions, thereby improving the frequency dynamics on the rectifier side. The four-state model is linearized to ascertain the interaction between rectifier and inverter-side frequencies and analytical expression for the frequency dynamics in terms of gains of the frequency controller at the rectifier station is derived. Moreover, the proposed reduced-order model shows the implications of frequency droop control of the wind farms in improving frequency dynamics on both rectifier and inverter sides. Expressions for 'synchronizing' and 'damping torque' contribution from HVDC and wind farm are also established. The analytical expressions and the effectiveness of the proposed strategies are validated through nonlinear time-domain simulations.**

***Index Terms*—Weak Grid, Averaged Model, Coupling, Firing Angle Correction, Droop, LCC, HVDC, DFIG, Inertia**

NOMENCLATURE

Wind farm:

ω_r	rotor speed
V_w	wind speed
T_{mech}	mechanical torque from wind
H_{WF}	total inertia constant of the multi-mass turbine
K_{opt}	constant for maximum power point tracking
R_{wind}	droop constant of the wind farm
P_{WF}	power output of the wind farm

HVDC:

Subscripts	r and i are used for the rectifier and the inverter
R_c	equivalent commutating resistance
E_{ac}	AC-side voltage phasor magnitude
E_{ac}^o	AC-side nominal voltage magnitude
I_{dr}/I_{di}	rectifier/inverter DC current
v_{dr}/v_{di}	rectifier/inverter DC voltage
α/γ	firing/extinction angle
α_r^*	firing angle before the correction strategy
R_{dc}	lumped DC transmission line resistance
R_H	$R_{cr} - R_{ci} + R_{dc}$
x_{rf}	state of rectifier-station frequency controller
K_{pf}, K_{if}	rectifier frequency controller gains
P_{HVDC_IN}	rectifier-side power
P_{HVDC_OUT}	inverter-side power

Generators:

Subscripts 1 and 2 are used for the rectifier and the inverter-side generators

H_G	inertia constant of the AC grid
R_{gov}	droop constant
ω	rotor speed
ω^*	reference synchronous speed
P_L	load on the inverter-side
T_{mech}	mechanical torque input

The authors are with School of Electrical Engineering and Computer Science, Pennsylvania State University, State College, PA, USA (e-mail: *suv66@psu.edu* and *nuc88@engr.psu.edu*).

Financial support from NSF Grant Award 1656983 is gratefully acknowledged.

I. INTRODUCTION

A significant portion of wind power generation in the US Midwest was considered in the 2008 US Department of Energy (DoE) report [1] due to high wind energy potential in that region. A recent example is the Rock Island Clean Line project [2] that proposes to deliver $3,500$MW of wind power from North-East Iowa to Illinois and other states to the east using a 500-mile overhead Line Commutated Converter (LCC)-based HVDC system. In this case, the Voltage Source Converter (VSC) technology could not match the high power rating demanded by the wind farms. According to the information presented on the Rock Island Clean Line project in [3], the rectifier-side AC system has wind farms, which are connected to two 345-kV substations. One is Substation OBRIEN, which is 6km away and the other is Substation RAUN, which is 97km away from the rectifier station. This is representative of a weak local AC grid hosting a wind farm interconnection with the LCC-HVDC rectifier station. Research on a scenario like this is of significant importance since a growing number of systems in the US and all over the world are experiencing interconnection of wind farms to such remote grids. This is the subject matter of our work as illustrated in Fig. 1.

Quite a few papers presented research on offshore wind farms (OWFs) connected to LCC-HVDC delivery systems [4]–[13]. However, due to stringent footprint requirements, LCC-HVDC

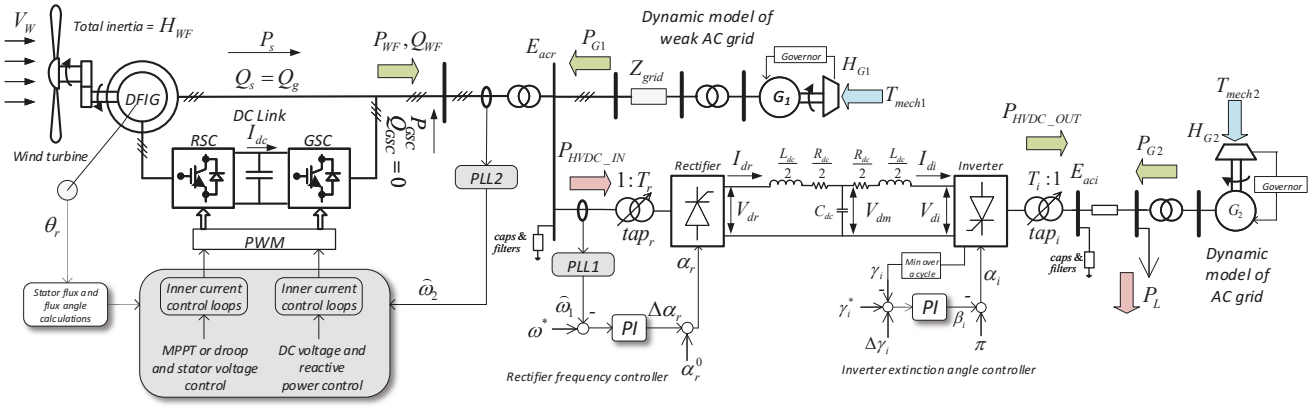

Fig. 1. Schematic of the DFIG-based wind farm connected to LCC-HVDC in a weak AC grid represented by a dynamic model. The 500-KV, 1000-MW LCC-HVDC rectifier station operates in a constant frequency control mode. Dynamic model of the inverter-side AC grid is also considered.

is ruled out, and the VSC technology is preferred for OWFs. Li et-al in [4] presented the damping enhancement and mitigation of the power fluctuations of a Doubly-Fed Induction Generator (DFIG)-based OWF. References [5]–[7] reported integration of OWFs to the onshore grid via LCC-HVDC system and the control coordination thereof. However, these papers did not present any notion of the coupling between real power–frequency ($P-f$) and reactive power–voltage ($Q-V$) channels in such systems and develop further insight into the root-cause of the dynamic behavior.

Bozhko et-al [8], [9] and Zhou et-al [11], [12] introduced a STATCOM in the offshore platform for providing voltage support at the PCC. Li et-al [13] developed an analytical formulation of DFIG-based OWFs operating under grid-connected mode. The contribution of this important work [13] was to design the LCC-HVDC frequency controller. However, the frequency dynamics of the inverter side and the coupling phenomenon were not presented or considered.

A few papers [14]–[17] reported research on the interconnection of DFIG-based wind farms with LCC-HVDC systems for onshore applications. References [14], [15] focused on frequency support from DFIG-based wind farms through LCC-HVDC link to the AC grid in the inverter side. Reference [16] oversimplified the inverter model and represented it by a DC voltage source. Yin et-al in [17] considered a very strong grid in the rectifier side with a synchronous generator connected to the terminal of the LCC-HVDC station. In [18], the rectifier station was operated with a constant frequency control and the impacts of low inertia constant and Effective Short Circuit Ratio (ESCR) were studied. However, the inverter-side AC grid was modeled as an ideal voltage source. Clearly, none of the papers have studied the effects of coupling between the rectifier-side and the inverter-side frequency dynamics.

This paper is an attempt to provide mathematical description of the coupling between frequency dynamics of the two AC systems interacting through LCC-HVDC where the rectifier side is interfaced with a weak AC system and a DFIG-based wind farm, see Fig. 1. The HVDC rectifier station operates in the frequency control mode as in reference [18]. To that end, a simple four-state nonlinear model is derived which is representative of the dynamics in the $P-f$ channel. Therefore, we expect the frequency dynamics obtained from the full-order model to be similar to that of the four-state nonlinear model. However, upon experimentation, an interesting coupling phenomenon between the $P-f$ and the $Q-V$ channels is observed. This complex $P-f$ and $Q-V$ interaction is not just present within the rectifier-side AC grid, but it propagates to both the grids through LCC-HVDC. As a result, instead of frequency dynamics as observed in the four-state model, an unfavorable frequency dynamics is observed in the full-order model.

To overcome this issue, a firing angle correction strategy is proposed, which decouples the $P-f$ and $Q-V$ interactions by desensitizing the LCC-HVDC power from the AC voltage variations at its terminals. It is shown that the correction strategy improves the frequency dynamics of the full-order model, which closely matches the response of the four-state nonlinear model representing the $P-f$ channel. The effectiveness of the correction strategy is validated through time-domain simulations of the full-order model equipped with correction strategy considering various disturbances.

Further, the proposed four-state model is linearized to ascertain the interaction between the rectifier and inverter-side frequencies and an analytical expression for the frequency response in terms of gains of the frequency controller at the rectifier station is derived. The proposed reduced-order model also shows the implications of frequency droop control of the wind farms and frequency control of HVDC on the 'synchronizing' and the 'damping' torque of rectifier-side generator. The analytical expressions and the insights are validated through nonlinear time-domain simulations of the full-order model equipped with the firing angle correction strategy considering various disturbances.

II. Full-order State-space Model of the System

The full-order nonlinear state-space averaged phasor model of the power system shown in Fig. 1 is derived in the form of the following Differential and Algebraic Equations (DAEs):

$$\begin{aligned} \dot{x} &= f(x,u,z) \\ 0 &= g(x,u,z) \end{aligned} \tag{1}$$

where x, u, and z are the state-variables, input variables, and algebraic variables, respectively. The rectifier and the inverter-side AC systems include synchronous generators G_1 and G_2,

which are represented using sixth-order subtransient models along with turbines, governors, and DC1A exciters. For this study, an inertia constant H_{G1} of 1.5s and an ESCR of 0.52 are considered to represent a weak rectifier-side AC system, while an inertia constant H_{G2} of 7.0s is assumed for representing a strong inverter-side AC grid that also includes a load center as shown in Fig. 1. The rectifier-side AC system includes a DFIG-based wind farm represented by an aggregated model. The wind farm considers a two-mass wind turbine model, a fourth order subtransient model of induction machine, and grid-side and rotor-side converts represented by averaged models along with inner current control loops. In addition, DC-link dynamics and the converter tie-reactor dynamics are also taken into account. The LCC HVDC converters are represented by standard algebraic models, while the DC transmission line is modeled by differential equations. As in [18], the rectifier station operates in a frequency control mode, where the controller parameters $K_{pf} = 0.0008$ and $K_{if} = 0.0007$ are chosen, see Fig. 1. Further details of the rectifier-side AC system and HVDC models can be found in [18] and are not repeated here due to space restrictions.

III. Proposed Four-State Nonlinear Model

We propose a four-state nonlinear model to help develop a deeper understanding of the interaction between frequencies of the rectifier-side and the inverter-side AC grids. In addition, a complex frequency-voltage coupling phenomenon that is propagated to both the grids through LCC-HVDC is explained with the help of the four-state model. We also demonstrate other applications in later sections, none of which can be achieved with the full-order model.

The following assumptions are made while deriving the four-state nonlinear model:

- AC network equations are not considered. Instead, real power balance equations obeying the network structure are considered.
- The AC system losses including losses in the lines, transformers, DFIG, and both the generators are neglected.
- It is assumed that the fast-acting power electronic control of the DFIG tracks the reference electrical torque instantaneously.
- Only the swing dynamics of the synchronous generators are considered.
- The PLL dynamics and the DC line dynamics of LCC-HVDC are neglected, and only DC line resistance is considered.
- The inverter-side control is assumed to tightly regulate the extinction angle at a constant value.

Unless otherwise stated, except for the notations mentioned under the Nomenclature, the rest are standard and self-explanatory.

With the above assumptions, the derivation begins from the power balance equations at PCC in the rectifier side and the load bus on inverter side as shown in Fig. 1,

$$\begin{aligned} P_{G1} + P_{WF} &= P_{HVDC\_IN} \\ P_{G2} + P_{HVDC\_OUT} &= P_L \end{aligned} \tag{2}$$

Considering the swing dynamics of the two synchronous machines and substituting powers P_{G1} and P_{G2} based on the above power balance equations,

$$\begin{aligned} \dot{\omega}_1 &= \tfrac{1}{2H_{G1}\omega_1}(P_{mech1} - P_{G1}) \\ &= \tfrac{1}{2H_{G1}\omega_1}(T_{mech1}\omega_1 + \tfrac{\omega^* - \omega_1}{R_{gov1}} + P_{WF} - P_{HVDC\_IN}) \\ \dot{\omega}_2 &= \tfrac{1}{2H_{G2}\omega_2}(P_{mech2} - P_{G2}) \\ &= \tfrac{1}{2H_{G2}\omega_2}(T_{mech2}\omega_2 + \tfrac{\omega^* - \omega_2}{R_{gov2}} + P_{HVDC\_OUT} - P_L) \end{aligned} \tag{3}$$

Here, ω^* is the synchronous speed, ω_1 and ω_2 are the rotor speeds, R_{gov1} and R_{gov2} are governor droop coefficients, and H_{G1} and H_{G2} are the inertia constants of generators G_1 and G_2, respectively. State variables ω_1 and ω_2 represent the angular frequencies of the rectifier and inverter AC grids.

□ *Remark I:* Note that the power angle (δ) states are not required in this model due to the following reasoning. Consider a case where a load (time-varying or otherwise) is connected to a single synchronous generator. If a classical two-state model is used, during the process of simulation, the power angle is generated. However, considering voltage behind the transient reactance as the reference voltage, there is no need to use δ in the dynamic simulation. Thus, in this particular situation, δ becomes a redundant state. Similar is the situation for the model considered in this work. It could be viewed as two AC systems such that in each system, a generator is connected to a (time-varying) load. Therefore, the δ states are not considered in modeling. □

In order to obtain the expression for the wind farm electrical power output, we use the assumption that the reference electrical torque ($T_e = K_{opt}\omega_r^2$) for DFIG is tracked instantaneously by the fast acting controls. Therefore, $P_{WF} = T_e\omega_r = K_{opt}\omega_r^3$. Moreover, the mechanical dynamics of the wind farm can be represented by the following equation,

$$\dot{\omega}_r = \tfrac{1}{2H_{WF}}[T_{tur}(V_w, \omega_r) - T_e] \tag{4}$$

Here, H_{WF} is the total inertia of the rotor and the turbine, and the mechanical torque input T_{tur} depends on wind speed V_w and rotor speed ω_r.

□ *Remark II:* A multi-mass model of the turbine-DFIG interface is necessary for studying phenomena involving the torsional mode of oscillation. Once such example is subsynchronous torsional interaction. Such a study is not of interest in this paper. Note that, the detailed model of the DFIG considers a 2-mass representation - please see reference [18]. As shown in [18], the torsional mode is not observable in the frequency dynamics of the rectifier-side. This is because of the fast converter controls that effectively decouples the mechanical side from the electrical side, which is a well-understood phenomenon. Therefore, a lumped one mass model is adequate for the four-state representation. □

The expressions for the DC voltages are given by,

$$\begin{aligned} V_{dr} &= \bar{V}_{or}E_{acr}\cos\alpha_r - R_{cr}I_{dr} \\ V_{di} &= \bar{V}_{oi}E_{aci}\cos\gamma_i - R_{ci}I_{di} \end{aligned} \tag{5}$$

where, $\bar{V}_{or} = \frac{3\sqrt{2}BT_r tap_r}{\pi}$ and $\bar{V}_{oi} = \frac{3\sqrt{2}BT_i tap_i}{\pi}$, and α_r is the firing angle of the rectifier, and γ_i is the extinction angle of the inverter. Since γ_i is assumed to be constant, let $\bar{V}_{oi}E_{aci}\cos\gamma_i = V_i$ and for simplicity let, $R_{cr} - R_{ci} + R_{dc} = R_H$. Furthermore, α_r is obtained from the frequency controller

in the rectifier station as shown in Fig. 1. Therefore we hav

$$\alpha_r = \alpha_{ro} + K_{pf}(\omega^* - \omega_1) + K_{if}x_{rf} \quad (6$$

where, x_{rf} is the integrator state, K_{pf} and K_{if} are th proportional and integral gains of the PI controller. Th expression for DC current is obtained as,

$$I_{dr} = I_{di} = \frac{(\bar{V}_{or}E_{acr}\cos\alpha_r - \bar{V}_{oi}E_{aci}\cos\gamma_i)}{R_{cr}-R_{ci}+R_{dc}} = \frac{(\bar{V}_{or}E_{acr}\cos\alpha_r - V$$

From above, the expressions for HVDC power inp P_{HVDC_IN} and power output P_{HVDC_OUT} shown in Fig. are obtained as,

$$P_{HVDC\_IN} = V_{dr}I_{dr} = I_{dr}\bar{V}_{or}E_{acr}\cos\alpha_r - R_{cr}I_{dr}^2$$
$$= \frac{(\bar{V}_{or}E_{acr}\cos\alpha_r - V_i)}{R_H}\bar{V}_{or}E_{acr}\cos\alpha_r - \frac{(\bar{V}_{or}E_{acr}\cos\alpha_r - V_i)^2}{R_H^2}R$$
$$P_{HVDC\_OUT} = V_{di}I_{di} = V_iI_{di} - R_{ci}I_{di}^2$$
$$= \frac{(\bar{V}_{or}E_{acr}\cos\alpha_r - V_i)}{R_H}V_i - \frac{(\bar{V}_{or}E_{acr}\cos\alpha_r - V_i)^2}{R_H^2}R_{ci}$$

(8

Finally, upon replacing the expressions for powers in (and the expression for electrical torque in (4) and including th state equation of rectifier frequency controller, the ***proposed four-state nonlinear model can be summarized as:***

$$\begin{aligned}
\dot{\omega}_1 &= \frac{1}{2\omega_1 H_{G1}}\Big[T_{mech1}\omega_1 + \frac{\omega^*-\omega_1}{R_{gov1}} + K_{opt}\omega_r^3 \\
&\quad - \frac{(\bar{V}_{or}E_{acr}\cos\alpha_r - V_i)}{R_H}\bar{V}_{or}E_{acr}\cos\alpha_r \\
&\quad + \frac{(\bar{V}_{or}E_{acr}\cos\alpha_r - V_i)^2}{R_H^2}R_{cr}\Big] \\
\dot{\omega}_2 &= \frac{1}{2\omega_2 H_{G2}}\Big[T_{mech2}\omega_2 + \frac{\omega^*-\omega_2}{R_{gov2}} \\
&\quad + \frac{(\bar{V}_{or}E_{acr}\cos\alpha_r - V_i)}{R_H}V_i \\
&\quad - \frac{(\bar{V}_{or}E_{acr}\cos\alpha_r - V_i)^2}{R_H^2}R_{ci} - P_L\Big] \\
\dot{\omega}_r &= \frac{1}{2H_{WF}}\big[T_{tur}(V_w,\omega_r) - K_{opt}\omega_r^2\big] \\
\dot{x}_{rf} &= \omega^* - \omega_1
\end{aligned} \quad (9)$$

In this paper we will present the following applications of the proposed four-state nonlinear model:

- Application I: reveal voltage-frequency coupling phenomenon
- Application II: propose novel firing-angle correction strategy
- Application III: develop analytical insight and energy bound on frequency deviation

IV. Application I: Revealing Voltage-Frequency Coupling Phenomenon

Upon deriving the full-order model and the reduced four-state model, two experiments are performed, which reveals a new voltage-frequency coupling phenomenon that arises when LCC-HVDC is regulating the frequency in a weak grid i.e., a grid with low inertia constant and low ESCR. For these experiments, a pulse variation in wind speed as shown in Fig. 2(a) is considered as disturbance. Figure 3 shows the variations in E_{acr} and E_{aci} observed in the full-order model due to this disturbance. ***In Experiment-I, the four-state model assumes E_{acr} and E_{aci} to be constant, since the variations in these variables are small.***

Noting that the four-state model adequately captures the dynamics in the $P-f$ channel, we expect it to faithfully represent the frequency deviations. However, it will be observed from Experiment-I that the frequency dynamics obtained from the full-order model, which is expected to follow the four-state

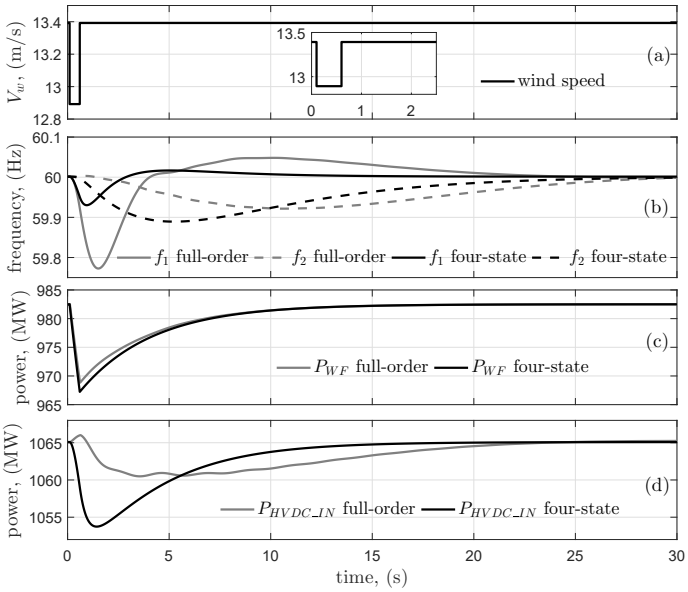

Fig. 2. Experiment-I: Comparison between the four-state nonlinear model and the full-order model responses following a pulse change in the wind speed.

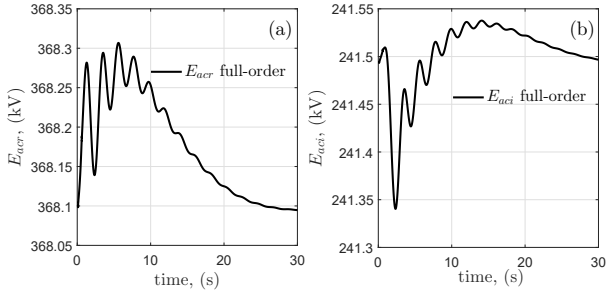

Fig. 3. Variations in the voltages at rectifier and inverter AC buses during the disturbance in wind speed, as obtained from the full-order model.

model's frequency dynamics; is out of synch and is worse in the rectifier side. It is logical to assume that such a deterioration in the frequency dynamics of the full-order model could be arising from the variations in E_{acr} and E_{aci}, which in turn can be treated as disturbance input hampering the performance of the rectifier-side frequency regulator.

To prove the above assertion, in Experiment-II, these variations are fed from the full-order model to the four-state model as shown in Fig. 4. It will be shown that the same unfavourable frequency dynamics are also observed in four-state model upon introducing these disturbances. Finally, based on these experimental results three conclusions will be drawn.

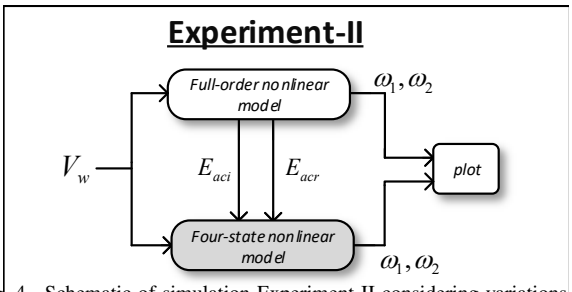

Fig. 4. Schematic of simulation Experiment-II considering variations of E_{acr} and E_{aci} from full-order model and feeding as input to four-state nonlinear model.

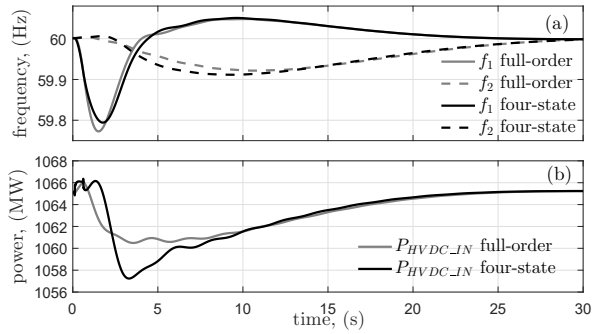

Fig. 5. Experiment-II: Similar unfavorable frequency dynamics as in the full-order model is obtained from the four-state model when the voltage variations are fed back from the full-order to four-state model as shown in Fig. 4.

A. Experiment-I: Without E_{acr} and E_{aci} Variations in Four-state Model

Since the variations in E_{acr} and E_{aci} are small, both are assumed to be constant at their pre-disturbance steady state values in the four-state model. Figure 2(b) shows the frequency dynamics of the four-state nonlinear model, which are expected in comparison with the unfavourable full-order model dynamics. ***We note that this unfavourable dynamics is particularly in relations to the frequency nadir, which is of major concern to the system operators.*** Despite the good match in the variation of P_{WF} (Fig. 2(c)), there is discrepancy in power flowing through HVDC at the rectifier as shown in Fig. 2(d). Therefore, this HVDC power discrepancy could be the reason behind an unfavourable frequency dynamics in the full-order model, which could be caused by the variations in E_{acr} and E_{aci}. To verify this, Experiment-II is performed as described next.

B. Experiment-II: with E_{acr} and E_{aci} Variations in Four-state Model

In this experiment, the variations of E_{acr} and E_{aci} that are obtained from the full-order model are fed to the four-state nonlinear model as shown in Fig. 4. It can be seen from Fig. 5(a) that the unfavourable frequency dynamics of the full-order model are replicated by the four-state nonlinear model. Also, power flowing into the HVDC rectifier shows similar variations, see Fig. 5(b). This implies that feeding the disturbances i.e., E_{acr} and E_{aci} variations into the four-state model affects the frequency regulator in the four-state model in the same way as the full-order model.

C. Analysis of Voltage-Frequency Coupling

Three important points can be concluded from the above experiments especially for a weak grid with low inertia constant and low ESCR,

1. The frequency dynamics of the system are governed by equations (3), which are dependent on the real powers. However, the HVDC real power is sensitive to voltage variations at the rectifier and inverter buses. The voltage variations depend on the reactive power flow. The reactive power consumed by the HVDC rectifier depends on α_r, which in turn is dependent on ω_1. *Therefore, the $P-f$ and the $Q-V$ dynamics are strongly interdependent in such weak grids and this complex coupling phenomenon is transferred to both AC grids via HVDC.*
2. As observed from Fig. 2, the frequency deviation in the rectifier side is much less in the four-state model, which considers only the $P-f$ dynamics as compared to the full-order model. Clearly, unfavourable frequency dynamics are caused by the complex coupling phenomenon explained above. Therefore, it is logical to conclude that desired dynamics of rectifier-side frequency can be achieved for a given set of frequency controller gains of HVDC if the $P-f$ and the $Q-V$ dynamics can be decoupled by some means.
3. The decoupling would involve desensitization of real power going into HVDC rectifier from the rectifier and the inverter bus voltage variations. We propose to achieve this by a correction strategy, which is described next.

V. Application II: Proposed Firing Angle Correction Strategy

In order to decouple the $P-f$ and the $Q-V$ dynamics, a new firing angle correction strategy is proposed. The aim is to make a correction to firing angle α_r such that the HVDC power becomes insensitive to the E_{acr} and E_{aci} variations. In case of the four-state model with the assumption of constant rectifier and inverter AC voltages equal to their respective nominal values, the HVDC power at the rectifier-end is given by,

$$P^*_{HVDC\_IN} = \frac{(\bar{V}_{or}E^0_{acr}\cos\alpha^*_r - V^0_i)}{R_H}\bar{V}_{or}E^0_{acr}\cos\alpha^*_r - \frac{(\bar{V}_{or}E^0_{acr}\cos\alpha^*_r - V^0_i)^2}{R^2_H}R_{cr} \quad (10)$$

where, E^0_{acr} is the nominal voltage at the rectifier bus. Also, $V^0_i = \bar{V}_{oi}E^0_{aci}\cos\gamma^0_i$, where E^0_{aci} is the nominal voltage at the inverter bus and γ^0_i is the constant extinction angle maintained at the inverter-end. α^*_r is the firing angle output of the frequency controller at rectifier. We can argue that $P^*_{HVDC\_IN}$ is the desired rectifier-side power, which is insensitive to the variations in E_{acr} and E_{aci}.

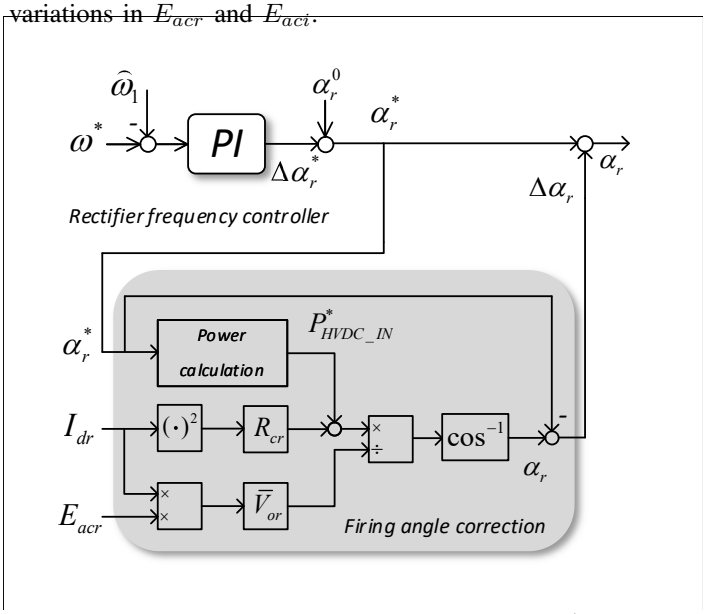

Fig. 6. Schematic of the firing angle correction strategy with α^*_r, E_{acr} and I_{dr} as input.

In actual case, due to variations in E_{acr} and E_{aci}, for any α_r the rectifier-side power is given by,

$$P_{HVDC\_IN} = V_{dr}I_{dr} = I_{dr}\bar{V}_{or}E_{acr}\cos\alpha_r - R_{cr}I^2_{dr} \quad (11)$$

Equating the above expression to $P^*_{HVDC\_IN}$ and solving for α_r, we obtain a firing angle, which when input to HVDC ensures that the rectifier-side power is $P^*_{HVDC\_IN}$. It implies that this power is insensitive to voltage variations at rectifier and inverter buses. Upon solving, the expression for α_r is obtained as,

$$\alpha_r = cos^{-1}\left(\frac{P^*_{HVDC\_IN}+R_{cr}I^2_{dr}}{I_{dr}\tilde{V}_{or}E_{acr}}\right) \quad (12)$$

The control block diagram of the proposed firing angle correction strategy along with the rectifier frequency controller is presented in Fig. 6. Please note that only locally measured signals E_{acr} and I_{dr} are used – there is no need to communicate E_{aci} from the remote inverter station.

A. Results & Analysis

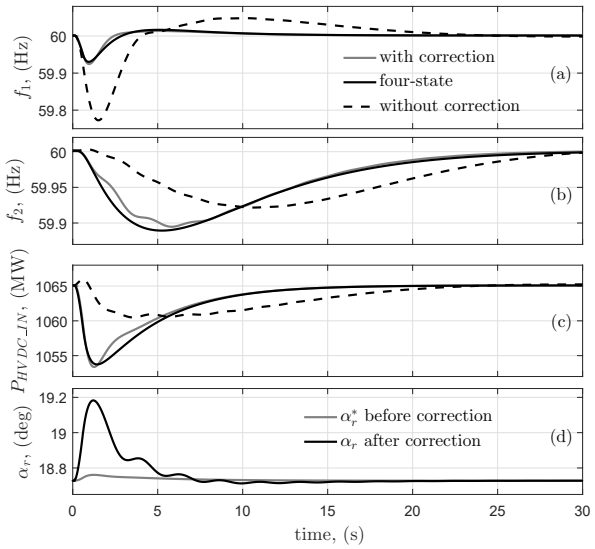

Fig. 7. Improved rectifier frequency dynamics obtained by implementing the firing angle correction strategy in the full-order model as shown in Fig. 6. Response from the four-state model with constant E_{acr} and E_{aci} is also shown.

1) Effectiveness of Proposed Method: Figure 7 (a) shows the reduction of the nadir and improved tracking of the rectifier-side frequency when the firing angle correction is applied. The same disturbance in wind speed as shown in Fig. 2 (a) is considered and the same PI controller gains are used in both cases. Figure 7 (d) shows the variation in the controller output α_r^* and the actual firing angle α_r, which is obtained by adding the correction term $\Delta\alpha_r$ to the controller output, see Fig. 6.

Figure 8 shows the frequency dynamics in the rectifier and the inverter side following a self-clearing fault in the rectifier-side AC system. Note that self-clearing fault implies that the fault does not need to be cleared by opening a circuit breaker, thereby separating an element (e.g. line, transformer, etc.). Such faults get automatically cleared, and are the most common type of faults. Also, plots of E_{acr} and E_{aci} are shown in Fig. 9 for more clarity. It can be clearly observed that the firing angle correction strategy is quite effective in improving the tracking performance of the rectifier-side frequency controller.

It can be seen that the improvement in the response of the rectifier-side frequency comes at an expense of slightly worse

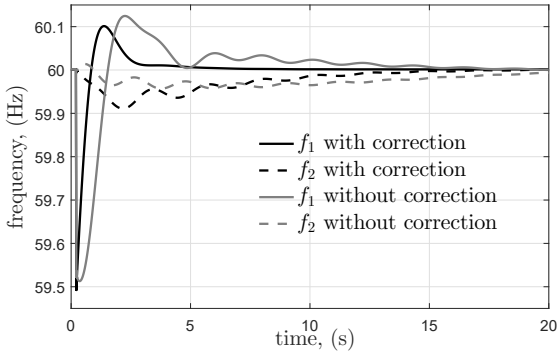

Fig. 8. Improved rectifier-side frequency dynamics following a self-clearing fault in the rectifier-side AC grid upon implementing the firing angle correction strategy.

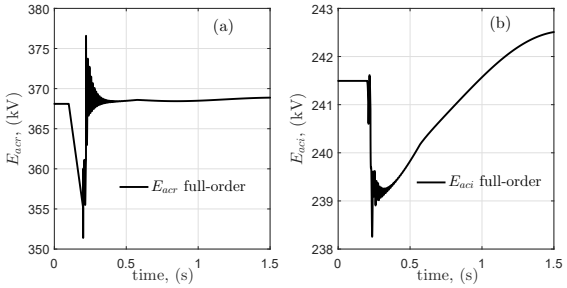

Fig. 9. Voltage variations after self-clearing fault in the rectifier-side AC system: (a) at the rectifier bus and (b) at the inverter bus. Rectifier is equipped with the firing angle correction control.

nadir of the frequency in the inverter-side AC system. However, a careful look at the response of f_2 reveals that firing angle correction brings this frequency back to the nominal value faster following both disturbances.

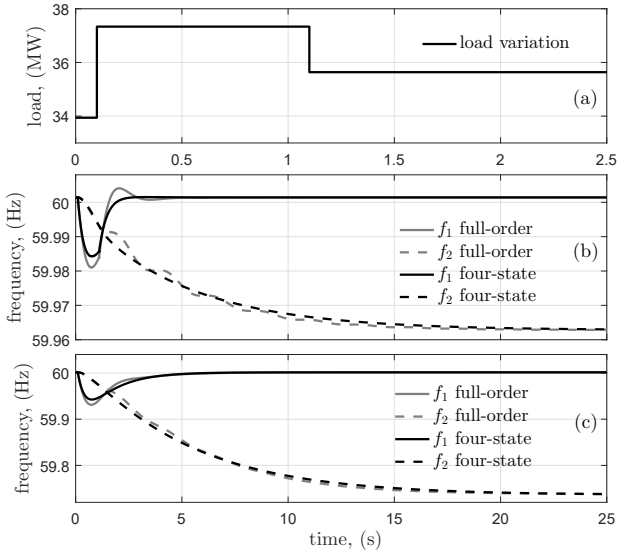

Fig. 10. Model validation for two scenarios. (i) Load change: (b) comparison of frequency deviation in the rectifier and the inverter-end following a change in real power consumption at the rectifier bus shown in (a). (ii) Generation change: (c) comparison of frequency deviation in the rectifier and the inverter-end following a 10 % step reduction in G_1's torque at t = 0.1s.

2) Modeling Adequacy of Four-State Model: Figure 7 shows a good match between the response of the four-state model

with constant E_{acr} and E_{aci}, and the response of the full-order model with firing angle correction for wind speed variation. Also, a good match in frequency dynamics as shown in Fig. 10 (b) is obtained following a change in real power consumption at the rectifier bus highlighted in Fig. 10 (a). Similarly, a good match as shown in Fig. 10 (c) is obtained following a 10 % reduction in generation on the rectifier side. Therefore, the proposed four-state model can adequately capture the frequency dynamics of the full-order system for disturbances like, wind speed variations, generation and load changes, when the full-order or the actual system is equipped with the firing angle correction strategy. However, for large disturbances, like AC-side fault, DC-side fault, loss of generation, etc. a detailed modeling is essential. Nonetheless, the frequency dynamics is improved even for disturbances like AC-side fault, see Fig. 8, by implementation of the correction strategy, which is inspired by the four-state model.

From now on, unless otherwise stated, all the time-domain responses will be presented from the full-order nonlinear model equipped with firing angle correction.

VI. Application III: Analytical Insight & Energy Bound on Frequency Deviation

The proposed four-state nonlinear model can be linearized to develop fundamental analytical insights that are not obtainable from the full-order linear model. Note that the four-state model is representative of the full-order system with firing angle correction.

A. Analytical Insight I: Decoupling of Rectifier-side Frequency Dynamics from Inverter-side Disturbance

The nonlinear state equations of the form $\dot{x} = f(x, u)$ in section II are linearized around the nominal operating point to obtain a linear state-space model of the form, $\dot{x} = Ax + Bu$. For linearization, torque references of both the generators, load on the inverter side, and wind speed are considered as input. Therefore, x and A are obtained as,

$$x = \begin{bmatrix} \Delta\omega_1 \\ \Delta\omega_2 \\ \Delta\omega_r \\ \Delta x_{rf} \end{bmatrix}; A = \begin{bmatrix} a_{11}^* + a'_{11}K_{pf} & 0 & a_{13} & a'_{14}K_{if} \\ a'_{21}K_{pf} & a_{22} & 0 & a'_{24}K_{if} \\ 0 & 0 & a_{33} & 0 \\ a_{41} & 0 & 0 & 0 \end{bmatrix} \tag{13}$$

Also, u and B are obtained as,

$$u = \begin{bmatrix} \Delta T_{mech1} \\ \Delta T_{mech2} \\ \Delta V_w \\ \Delta P_L \end{bmatrix}; B = \begin{bmatrix} b_{11} & 0 & 0 & 0 \\ 0 & b_{22} & 0 & b_{24} \\ 0 & 0 & b_{33} & 0 \\ 0 & 0 & 0 & 0 \end{bmatrix} \tag{14}$$

Analytical expressions for the elements of the A and the B matrices are presented in the Appendix. The dependence of the terms of A matrix on the proportional (K_{pf}) and the integral (K_{if}) gains of the frequency controller at the rectifier station is shown. From the locations of zeros in the A and the B matrices, we can develop the following fundamental insights:

- The dynamics of ω_1 is dependent on ω_1, ω_r, and x_{rf}, which are not affected by variations in ω_2. Therefore, disturbances on the inverter side does not directly affect ω_1, unless E_{aci} is so much out of range that the firing angle correction strategy fails.
- Based on the above, since changes in T_{mech2} and P_L cause variation in ω_2, they do not affect the dynamics of ω_1. Notably, dynamics in ω_2 is dependent on ω_1 and x_{rf}. *Therefore, as far as the frequency dynamics is concerned, the firing angle correction is allowing a one-way propagation of disturbance from the rectifier side to the inverter side, while firewalling the return path.*
- The above is not true for LCC-HVDC when traditional current order control is present at the rectifier-side. In presence of sufficient reactive power compensation and traditional current control in the rectifier-side, there will be no one-way coupling from the rectifier-side frequency dynamics to the inverter-side. This is well-known, and can be found from literature; one of the early examples being [19].

TABLE I
Per-unit energy bound on $\Delta\omega_1$ and $\Delta\omega_2$ for different PI gains

PI gains, pu	bound: $\Delta\omega_1$	bound: $\Delta\omega_2$
$K_{pf} = 0.0004$, $K_{if} = 0.00035$	0.0161	0.0656
$K_{pf} = 0.0008$, $K_{if} = 0.0007$	0.0088	0.0656

B. Analytical Insight II: Per-unit Energy Bound on Frequency Deviation

From the matrices A and B, transfer functions between $\Delta\omega_1$ and ΔV_w, and between $\Delta\omega_2$ and ΔV_w are derived as,

$$\begin{aligned} \frac{\Delta\omega_1(s)}{\Delta V_w(s)} &= \frac{b_{33}a_{13}s}{(s-a_{33})[s(s-a_{11}^*-a'_{11}K_{pf})-a_{41}a'_{14}K_{if}]} \\ \frac{\Delta\omega_2(s)}{\Delta V_w(s)} &= \frac{b_{33}a_{13}(a_{21}s+a'_{24}a_{41}K_{if})}{(s-a_{22})(s-a_{33})[s(s-a_{11}^*-a'_{11}K_{pf})-a_{41}a'_{14}K_{if}]} \end{aligned} \tag{15}$$

Using the transfer functions we can determine the $\mathcal{H}_\infty$ norm, which gives us a bound on the per unit (pu) energy of the variation in frequencies of the rectifier-side and inverter-side grids for a unit variation in energy of the wind speed in m/sec. Table I shows that the pu energy bound on $\Delta\omega_1$ is lower when higher gains are used for the frequency controller while the pu energy bound on $\Delta\omega_2$ remains unchanged.

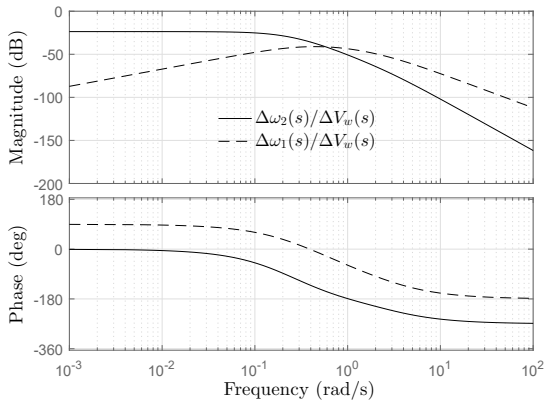

Fig. 11. Bode plot of the transfer functions from wind speed to ω_1 and ω_2.

Also, Fig. 11 shows the bode plot of the two transfer functions with nominal values of K_{pf} and K_{if}. Please note that frequency-domain analysis is now being considered. Therefore, the input, which is the wind speed variation is in frequency-domain i.e., the Fourier transform of the wind speed variation,

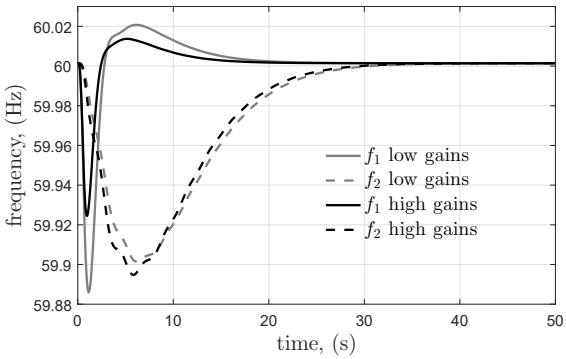

Fig. 12. Effect of increasing PI gains (Table I) in the frequency controller at the rectifier station: response from full-order model with firing angle correction.

is taken into account. Also notice that the energy bound ($\mathcal{H}_\infty$ norm) on the variation in ω_2 is the DC gain (maximum magnitude) of the transfer function $\frac{\Delta\omega_2(s)}{\Delta V_w(s)}$. This shows that:

- Very low frequency (less than 0.1Hz) variations in wind speed affects the rotational kinetic energy of the generator on the inverter side, while the rectifier frequency remains unaffected.
- We observe a crossover around 0.1Hz frequency. This implies, wind speed fluctuations at higher than 0.1Hz frequency will affect f_1 more than f_2.

Figure 12 shows that the rectifier-side frequency dynamics improves when higher PI gains are used, see Table I. The same pulse change in the wind speed as in Fig. 2 (a) is applied as the disturbance. However, a high gain controller leads to higher loop transfer function, which negatively impacts the robust stability due to system noise, and uncertain and un-modeled plant dynamics when operating conditions change. Also, it leads to higher control effort. Moreover, this does not improve the inverter-side frequency dynamics. In order to improve the frequency dynamics on both the grids by using low PI gains, droop control of wind farm is considered, which is described next.

C. Analytical Insight III: Droop Control of Wind Farm

Usually, frequency droop control in wind farms will need a deloaded operation. However, with the frequency controller at the rectifier station maintaining the frequency at a constant value in steady state – the frequency droop control is effective only under dynamic condition. Therefore, it is not essential to operate the wind farm in deloaded condition.

For implementing the droop control the electrical torque reference of the DFIG is modified as,

$$T_e^* = K_{opt}\omega_r^2 + \frac{\omega^* - \omega_1}{R_{wind}} \tag{16}$$

where, R_{wind} is the wind droop constant. In the full-order model ω_1 is measured using the PLL located at the DFIG bus, which usually measures angle of the voltage for DFIG controls. Also, for the four-state model the wind farm electrical power output is modified as $P_{WF} = T_e^*\omega_r$.

With the new four-state nonlinear equations, upon linearization we get the A matrix as,

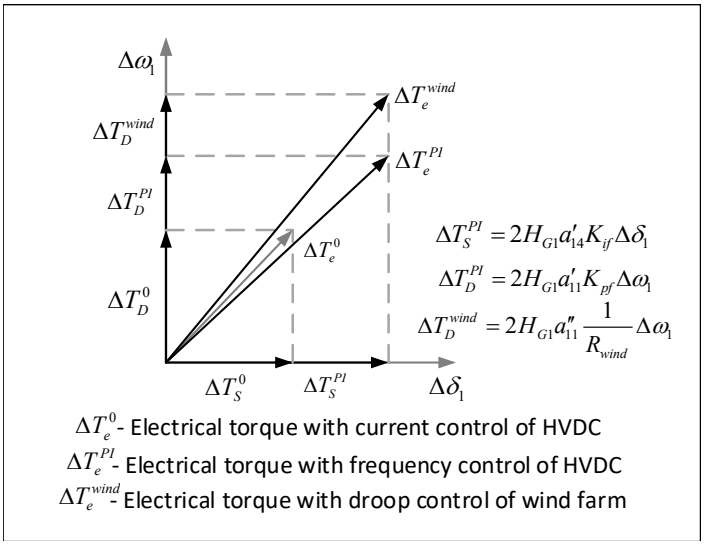

Fig. 13. Impacts of frequency control of rectifier station and frequency droop control of wind farm on damping torque and synchronizing torque of G_1.

$$A = \begin{bmatrix} a_{11}^* + a''_{11}\frac{1}{R_{wind}} + a'_{11}K_{pf} & 0 & a_{13} & a'_{14}K_{if} \\ a'_{21}K_{pf} & a_{22} & 0 & a'_{24}K_{if} \\ a'_{31}\frac{1}{R_{wind}} & 0 & a_{33} & 0 \\ a_{41} & 0 & 0 & 0 \end{bmatrix} \tag{17}$$

while, B, x and u remain the same. Also as explained in section VI-A, based on the zeros in the A matrix, HVDC is acting as a one way firewall thereby, protecting the rectifier-side grid from the disturbances in the inverter-side grid. With this, the following new insights can be derived:

- In the previous case dynamics of ω_r was *decoupled* from other dynamic states. In presence of droop control, the wind farm's rotor dynamics gets coupled with ω_1 and in turn with the rectifier station PI controller dynamics as well. This is due to the term $a'_{31}\frac{1}{R_{wind}}$ appearing in the A matrix.
- A term $a''_{11}\frac{1}{R_{wind}}$ is appearing in the A matrix, which could improve the dynamics of ω_1. Improvement in ω_1 could possibly improve the dynamics of ω_2 as well. Note that this improvement in the dynamics is obtained without the deloaded operation of the wind farm.

In the case of droop control of wind farm, from the matrices A and B, transfer functions between $\Delta\omega_1$ and ΔV_w, and between $\Delta\omega_2$ and ΔV_w are derived as,

$$\begin{aligned} \frac{\Delta\omega_1(s)}{\Delta V_w(s)} &= \frac{b_{33}a_{13}s}{[s(s-a_{11})(s-a_{33}) - sa_{13}a_{31} - (s-a_{33})a_{14}a_{41}]} \\ \frac{\Delta\omega_2(s)}{\Delta V_w(s)} &= \frac{b_{33}a_{13}(a_{21}s + a_{24}a_{41})}{(s-a_{22})[s(s-a_{11})(s-a_{33}) - sa_{13}a_{31} - (s-a_{33})a_{14}a_{41}]} \end{aligned} \tag{18}$$

Note that by setting a_{31} to '0', transfer functions presented in (15) are obtained. Please see Appendix for parameters.

TABLE II
DAMPING TORQUE COEFFICIENTS K_d OF G_1

PI gains, pu	R_{wind}	K_d
$K_{pf} = 0.0001333$, $K_{if} = 0.0001167$	5	14.5299
$K_{pf} = 0.0008$, $K_{if} = 0.0007$	no droop	10.3209

D. Analytical Insight IV: Synchronizing and Damping Torque

The state variable x_{rf} is obtained by integration of $\omega^* - \omega_1$, so Δx_{rf} represents $\Delta\delta$ of the machine. Therefore, from the first row of the A matrix, we have $2H_{G1}a'_{14}K_{if}\Delta\delta_1$ as the additional synchronizing torque and $2H_{G1}a'_{11}K_{pf}\Delta\omega_1$ as additional damping torque from the rectifier frequency control, and $2H_{G1}a''_{11}\frac{1}{R_{wind}}\Delta\omega_1$ as another additional damping torque from frequency droop control of wind farm – see Fig. 13. The increase in damping torque contribution from G_1 in presence of droop control will further enhance damping, which will be shown later.

VII. Results & Analysis

In order to improve the frequency dynamics in both the grids, droop control of wind farm is considered in this section. As before, the results are demonstrated using the full-order model equipped with firing angle correction strategy. Lower gains of the frequency controller were chosen when droop control is used, so as to match the frequency nadir in the rectifier side in the absence of droop, see Table II.

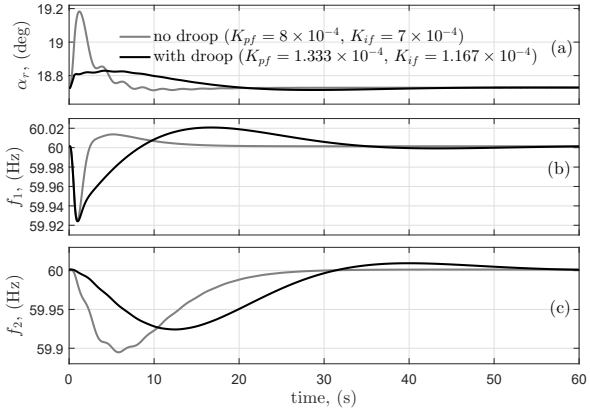

Fig. 14. Frequency dynamics due pulse reduction in wind speed, presenting improvement on both inverter and rectifier sides dynamics upon implementation of the frequency droop control in wind farm.

Figure 14 presents the dynamics following a pulse reduction in wind speed, as shown in Fig. 2 (a). It is clear from Fig. 14 (b) that the frequency nadir on the rectifier side is the same with and without frequency droop control of wind farm. However,

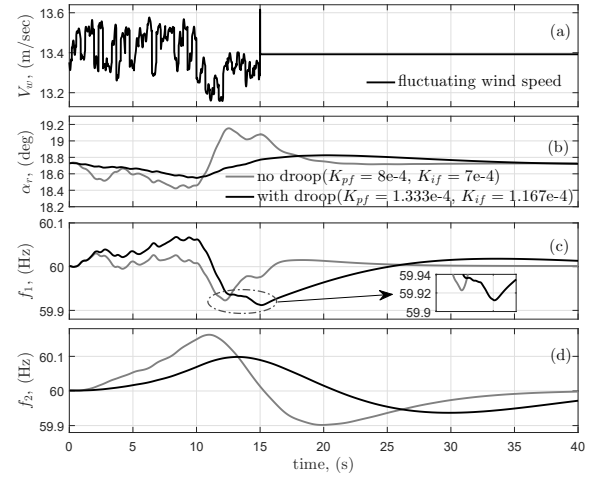

Fig. 15. Frequency dynamics due to fluctuations in the wind speed. Improvement on inverter-side dynamics, upon implementation of the frequency droop control in wind farm.

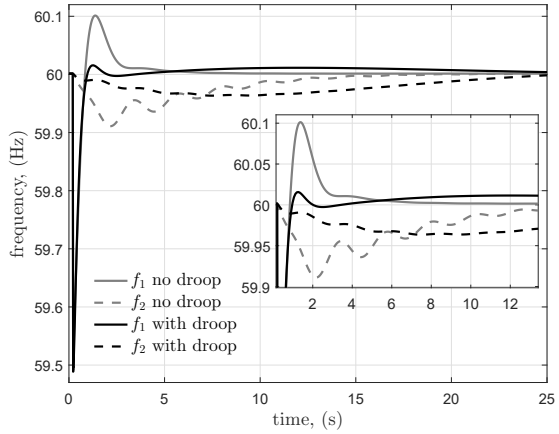

Fig. 16. Improvement in frequency dynamics following a rectfier-side self-clearing fault with the implementation of frequency droop control in wind farm. Improved damping in f_2 is observed with droop.

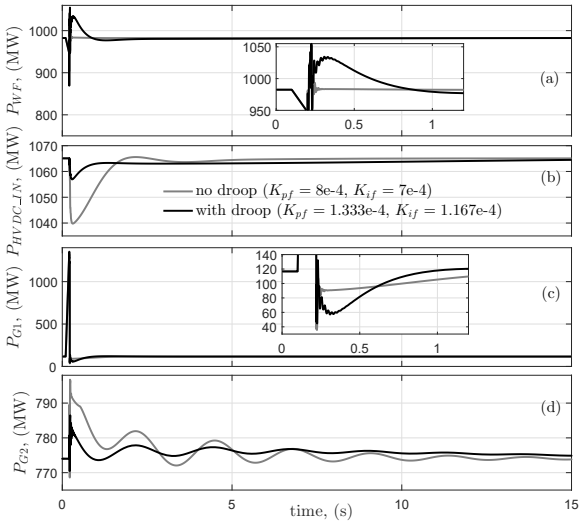

Fig. 17. Variation in powers of: (a) Wind farm, (b) HVDC rectifier-side input, (c) Rectifier-side generator and (d) Inverter-side generator following a rectifier-side self-clearing fault. Improved damping in P_{G2} with droop is observed.

Fig. 14 (c) shows that the frequency nadir on the inverter side is improved with the implementation of the frequency droop control of the wind farm. Similar observations can be made when fluctuating wind speeds as shown in Fig. 15 (a) is considered. This is because the frequency nadir is of more concern than the frequency overshoot to the system operators as it directly affects under-frequency tripping. Therefore, a zoomed portion of the rectifier-side frequency nadir is presented in Fig. 15 (c) to prove that the nadir is almost the same with or without frequency droop control. However, frequency dynamics on the inverter side (Fig. 15 (d)) is improved with frequency droop control of wind farm. Lower PI gains are used in presence of frequency droop control. As a result, the variations in firing angle (α_r) is less when droop control is applied, see Figs 14 (a) and 15 (b).

Figure 16 shows the frequency deviation following a high impedance self-clearing fault in the rectifier-side AC system. Although, during the fault the responses are the same, after the fault is cleared, the frequency excursion on both rectifier side

and inverter side are more contained in presence of frequency droop control as shown in the zoomed part of Fig. 16. Figure 17 shows different system variables following the fault. Improved system damping is observed from P_{G2} as well as f_2 in Fig. 16 in presence of droop control. This is in-line with damping torque analysis of section VI-D and calculated values of K_d presented in Table II. Note that the source of system damping is the damping torque contribution from generators. In this case, damping torque contribution from $G1$ increases in presence of droop control, thereby improving the system damping ratio. This gets reflected in the entire system response, which is not just confined to the rectifier-side. As a result, improvement is also observed in the inverter-side response, like P_{G2} and f_2.

VIII. Conclusion

A fourth-order nonlinear dynamic model of AC grids in rectifier and inverter side of LCC-HVDC interfacing a DFIG-based wind farm was proposed. The proposed model considered coupling between frequency dynamics of the weak rectifier-side system with the inverter-side grid where the rectifier operates in frequency control mode. This model revealed a complex coupling between frequency and voltage in the rectifier side which propagates to the inverter end, thereby, deteriorating frequency dynamics. A firing angle correction strategy was proposed to desensitize the frequency dynamics from voltage to improve the performance. Further, a reduced-order linearized model developed fundamental insights including synchronizing and damping torque contributions from HVDC, energy bound on frequency deviation, and a unidirectional rectifier-inverter frequency coupling. Frequency droop control of wind farm showed improvement in both the rectifier and inverter-side frequency dynamics. The proposed four-state model has potential applications in sophisticated control design. For example, this reduced-order model can be useful while applying most of the modern control theories (e.g. LQG, LQR, $\mathcal{H}_\infty$, model predictive controls, etc.) where the controller could have at least as many states as the plant.

Appendix I

□ Inverter-side system: $H_{G2} = 7.0s$, $R_{gov2} = 0.005(Hz/pu - MW)$, $P_L = 1700MW$, nominal $P_{G2} = 774.01MW$ and rating of $G_2 = 900MW$.

□ The expressions for the terms in the A and B matrices are presented below (superscript '0' denotes nominal condition):

$$a^*_{11} = -\frac{1}{2H_{G1}(\omega^0_1)^2}\{\frac{\omega^0_1}{R_{gov1}} + K_{opt}(\omega^0_r)^3 - I^0_d\bar{V}_{or}E_{acr}\cos\alpha^0_r + R_{cr}(I^0_d)^2\}$$

$$a'_{11} = -a'_{14} = -\frac{1}{2H_{G1}\omega^0_1}\{(I^0_d\bar{V}_{or}E_{acr}\sin\alpha^0_r + \frac{(\bar{V}_{or}E_{acr})^2\sin 2\alpha^0_r}{2R_H} - \frac{2R_{cr}I^0_d\bar{V}_{or}E_{acr}\sin\alpha^0_r}{R_H}\}$$

$$a''_{11} = -\frac{\omega^0_r}{2H_{G1}\omega^0_1}; a_{13} = \frac{3K_{opt}(\omega^0_2)^2}{2H_{G1}\omega^0_1}$$

$$a'_{21} = -a'_{24} = \frac{1}{2H_{G2}\omega^0_2R_H}(V_i\bar{V}_{or}E_{acr}\sin\alpha^0_r - 2R_{ci}I^0_d\bar{V}_{or}E_{acr}\sin\alpha^0_r)$$

$$a_{22} = -\frac{1}{2H_{G2}(\omega^0_2)^2}(\frac{\omega^0_2}{R_{gov2}} + I^0_dV_i - R_{ci}(I^0_d)^2 - P^0_L)$$

$$a'_{31} = \frac{1}{2H_{WF}}(\frac{\partial T_{mech}(V_w,\omega_r)}{\partial\omega_r}\Big|_{(V^0_w,\omega^0_r)} - 2K_{opt}\omega^0_r)$$

$$a_{41} = -1; b_{11} = \frac{1}{2H_{G1}}; b_{22} = \frac{1}{2H_{G2}}$$

$$b_{33} = \frac{1}{2H_{WF}}(\frac{\partial T_{mech}(V_w,\omega_r)}{\partial V_w}\Big|_{(V^0_w,\omega^0_r)}); b_{24} = \frac{-1}{2H_{G2}\omega^0_2}$$

$$a_{11} = a^*_{11} + a''_{11}\frac{1}{R_{wind}} + a'_{11}K_{pf}; a_{14} = a'_{14}K_{if}$$
$$a_{21} = a'_{21}K_{pf}; a_{24} = a'_{24}K_{if}; a_{31} = a'_{31}\frac{1}{R_{wind}}$$

References

[1] U.S. Department of Energy, Tech. Rep. May 2008. "20% wind energy by 2030: Increasing wind energy's contribution to U.S. electricity supply".
[2] Clean Line Energy, http://www.rockislandcleanline.com/site/home.
[3] A. Hernandez, R. Majumder, W. Galli, C. Bartzsch, D. Danis, A. Chaudhry, "Facilitating Bulk Wind Power Integration Using LCC HVDC," Rock Island Exhibit 2.19, CIGRE US National Committee 2013 Grid of the Future Symposium.
[4] L. Wang and K. H. Wang, "Dynamic stability analysis of a DFIG-based offshore wind farm connected to a power grid through an HVDC link," *IEEE Transactions on Power Systems*, vol. 26, no. 3, pp. 1501–1510, Aug 2011.
[5] D. Xiang, L. Ran, J. R. Bumby, P. J. Tavner, and S. Yang, "Coordinated control of an HVDC link and doubly fed induction generators in a large offshore wind farm," *IEEE Transactions on Power Delivery*, vol. 21, no. 1, pp. 463–471, Jan 2006.
[6] H. Yin, L. Fan, and Z. Miao, "Coordination between DFIG-based wind farm and LCC-HVDC transmission considering limiting factors," in *IEEE 2011 EnergyTech*, May 2011, pp. 1–6.
[7] H. Yin and L. Fan, "Modeling and control of DFIG-based large offshore wind farm with HVDC-link integration," in *41st North American Power Symposium*, Oct 2009, pp. 1–5.
[8] S. V. Bozhko, R. Blasco-Gimenez, R. Li, J. C. Clare, and G. M. Asher, "Control of offshore DFIG-based wind farm grid with line-commutated HVDC connection," *IEEE Transactions on Energy Conversion*, vol. 22, no. 1, pp. 71–78, March 2007.
[9] S. Bozhko, G. Asher, R. Li, J. Clare, and L. Yao, "Large offshore DFIG-based wind farm with line-commutated HVDC connection to the main grid: Engineering studies," *IEEE Transactions on Energy Conversion*, vol. 23, no. 1, pp. 119–127, March 2008.
[10] H. Zhou and G. Yang, "Control of DFIG-based wind farms with hybrid HVDC connection," in *2009 IEEE 6th International Power Electronics and Motion Control Conference*, May 2009, pp. 1085–1091.
[11] H. Zhou, G. Yang, and J. Wang, "Modeling, analysis, and control for the rectifier of hybrid HVdc systems for DFIG-based wind farms," *IEEE Transactions on Energy Conversion*, vol. 26, no. 1, pp. 340–353, March 2011.
[12] L. Ran, D. Xiang, L. Hu, and K. Abbott, "Voltage stability of an HVDC system for a large offshore wind farm with DFIGs," in *The 8th IEE International Conference on AC and DC Power Transmission*, March 2006, pp. 150–154.
[13] R. Li, S. Bozhko, and G. Asher, "Frequency control design for offshore wind farm grid with LCC-HVDC link connection," *IEEE Transactions on Power Electronics*, vol. 23, no. 3, pp. 1085–1092, May 2008.
[14] F. Lingling, M. Zhixin, and D. Osborn, "Wind farms with HVDC delivery in load frequency control," *IEEE Transactions on Power Systems*, vol. 24, no. 4, pp. 1894–1895, 2009.
[15] Z. Miao, L. Fan, D. Osborn, and S. Yuvarajan, "Wind farms with HVdc delivery in inertial response and primary frequency control," *IEEE Transactions on Energy Conversion*, vol. 25, no. 4, pp. 1171–1178, Dec 2010.
[16] M. Zhang, X. Yuan, J. Hu, S. Wang, S. Ma, Q. He, and J. Yi, "Wind power transmission through LCC-HVDC with wind turbine inertial and primary frequency supports," in *2015 IEEE Power Energy Society General Meeting*, July 2015, pp. 1–5.
[17] H. Yin, L. Fan, and Z. Miao, "Fast power routing through HVDC," *IEEE Transactions on Power Delivery*, vol. 27, no. 3, pp. 1432–1441, July 2012.
[18] A. Yogarathinam, J. Kaur, and N. R. Chaudhuri, "Impact of inertia and effective short circuit ratio on control of frequency in weak grids interfacing LCC-HVDC and DFIG-based wind farms," *IEEE Transactions on Power Delivery*, vol. 32, no. 4, pp. 2040–2051, Aug 2017.
[19] M. Klein, G. J. Rogers, and P. Kundur, "A fundamental study of inter-area oscillations in power systems," *IEEE Transactions on Power Systems*, vol. 6, no. 3, pp. 914–921, Aug 1991.

Sai Gopal Vennelaganti (S'16) received his Bachelors degree (B.Tech) in Electrical Engineering from Indian Institute of Technology Madras (IITM), Chennai, India in 2016. He joined the Ph.D. program of the Pennsylvania State University, University Park, PA in Fall 2016.

His research interests include power electronic control applications in Renewable Integration, HVDC, Multi-terminal HVDC, Power Quality, Electrical Drives, Hybrid Microgrids and Smart grids. He is currently working on modeling and control of Multi-terminal HVDC to resolve various challenges associated with it.

Nilanjan Ray Chaudhuri (S'08-M'09-SM'16) received his Ph.D. degree from Imperial College London, London, UK in 2011 in Power Systems. From 2005-2007, he worked in General Electric (GE) John F. Welch Technology Center. He came back to GE and worked in GE Global Research Center, NY, USA as a Lead Engineer during 2011-2014. Presently, he is an Assistant Professor with the School of Electrical Engineering and Computer Science at Penn State, University Park, PA. He was an Assistant Professor with North Dakota State University, Fargo, ND, USA during 2014-2016. He is a member of the *IEEE* and *IEEE PES*. Dr. Ray Chaudhuri is the lead author of the book *Multi-terminal Direct Current Grids: Modeling, Analysis, and Control* (Wiley/IEEE Press, 2014), and an Associate Editor of the IEEE TRANSACTIONS ON POWER DELIVERY. Dr. Ray Chaudhuri is the recipient of the National Science Foundation Early Faculty CAREER Award in 2016.